

Charge redistribution and the magnetoelastic transition across the first-order magnetic transition in (Mn,Fe)₂(P,Si,B)

Maschek, Michael; You, Xinmin; Boeije, Maurits; Chernyshov, D; van Dijk, Niels; Brück, Ekkes

DOI

[10.1103/PhysRevB.98.224413](https://doi.org/10.1103/PhysRevB.98.224413)

Publication date

2018

Document Version

Final published version

Published in

Physical Review B (Condensed Matter and Materials Physics)

Citation (APA)

Maschek, M., You, X., Boeije, M., Chernyshov, D., van Dijk, N., & Brück, E. (2018). Charge redistribution and the magnetoelastic transition across the first-order magnetic transition in (Mn,Fe)₂(P,Si,B). *Physical Review B (Condensed Matter and Materials Physics)*, *98*(224413), 1-8.
<https://doi.org/10.1103/PhysRevB.98.224413>

Important note

To cite this publication, please use the final published version (if applicable).
Please check the document version above.

Copyright

Other than for strictly personal use, it is not permitted to download, forward or distribute the text or part of it, without the consent of the author(s) and/or copyright holder(s), unless the work is under an open content license such as Creative Commons.

Takedown policy

Please contact us and provide details if you believe this document breaches copyrights.
We will remove access to the work immediately and investigate your claim.

Charge redistribution and the magnetoelastic transition across the first-order magnetic transition in $(\text{Mn,Fe})_2(\text{P,Si,B})$

M. Maschek,¹ X. You,¹ M. F. J. Boeije,¹ D. Chernyshov,² N. H. van Dijk,¹ and E. Brück¹

¹*Fundamental Aspects of Materials and Energy, Faculty of Applied Sciences, Delft University of Technology, Mekelweg 15, 2629 JB Delft, The Netherlands*

²*BM01, Swiss-Norwegian Beam Lines, European Synchrotron Radiation Facility, 71 Avenue des Martyrs, 38000 Grenoble, France*



(Received 25 July 2018; published 11 December 2018)

We used temperature dependent high-resolution x-ray powder diffraction and magnetization measurements to investigate structural, magnetic and electronic degrees of freedom across the ferromagnetic magnetoelastic phase transition in $\text{Mn}_1\text{Fe}_1\text{P}_{0.6-w}\text{Si}_{0.4}\text{B}_w$ ($w = 0, 0.02, 0.04, 0.06, 0.08$). The magnetic transition was gradually tuned from a strong first-order ($w = 0$) towards a second-order magnetic transition by substituting P by B. Increasing the B content leads to a systematic increase in the magnetic transition temperature and a decrease in thermal hysteresis, which is below 1 K for $w = 0.08$. Furthermore, the largest changes in lattice parameter across the magnetic transition occur for $w = 0$, which systematically becomes smaller approaching the samples with $w = 0.08$. Electron density plots show a strong directional preference of the electronic distribution around Fe, which indicates the forming of bonds between Fe atoms and Fe and P/Si in the paramagnetic phase. On the other hand, Mn shows no preferred directions. Due to the low B concentrations ($w < 0.08$), distortions of the lattice are limited. However, even small amounts of B strongly disturb the overall distribution of the electron density across the unit cell. Samples containing B show a strongly reduced change in the electron density compared to the parent compound without B. The magnetoelastic coupling shows a continuous weakening with the B content.

DOI: [10.1103/PhysRevB.98.224413](https://doi.org/10.1103/PhysRevB.98.224413)

I. INTRODUCTION

Growing energy demands and declining natural resources require the development of sustainable, clean and energy-efficient technologies. Magnetocaloric materials have great potential to efficiently exchange thermal energy and magnetic energy, because they generate heat when placed in a magnetic field. Upon removal of the field, the material cools down below the environmental temperature. Magnetic cooling and magnetic heat pumps are promising techniques due to their increased efficiencies, which can be 20–30% higher compared to conventional technologies [1–7]. In the reversed process, a temperature-induced magnetization change can be utilized to convert low-temperature waste heat ($< 80^\circ\text{C}$) into mechanical energy by thermomagnetic motors [8–14], which may further be converted into electricity. The utilization of the magnetocaloric effect (MCE) near room temperature could reduce the worldwide energy consumption and lower the emission of greenhouse gasses, due to significantly higher efficiencies and the use of environmentally friendly and abundantly available base materials.

The magnitude of the MCE crucially depends on the nature of the phase transition and the change in magnetization with temperature. A first-order magnetic transition (FOMT) is typically associated with a large jump in the magnetization and a discontinuous change in lattice parameters and volume across the Curie temperature T_C . Furthermore, a FOMT is generally accompanied by latent heat and thermal hysteresis. The MCE is maximized and results in an enhanced adiabatic temperature change in the form of a large latent heat, which is beneficial for magnetic cooling devices. However, the volume change

across T_C in a FOMT may damage the structural integrity of the material after multiple cycles and reduce longevity. On the other hand, a second-order magnetic transition (SOMT) does not involve a discontinuous jump in volume and is not accompanied by latent heat or hysteresis. Typically the change in magnetization is extended over a wider temperature range in a SOMT compared to a FOMT.

Close to a magnetic phase transition the (reversible) change in Gibbs free energy per unit volume ΔG can be described by the Landau-model [15]:

$$\Delta G = \frac{\alpha}{2}M^2 + \frac{\beta}{4}M^4 + \frac{\gamma}{6}M^6 - \mu_0HM, \quad (1)$$

where M is the magnetization and μ_0H is the applied magnetic field. Parameter $\alpha = \alpha_0(T - T_0)$ depends linearly on temperature with respect to a characteristic temperature T_0 . Parameters $\alpha_0 > 0$, β , $\gamma > 0$ are temperature-independent constants. Minimization with respect to the magnetization $M(\partial\Delta G/\partial M = 0)$ leads to the equation of state:

$$\alpha + \beta M^2 + \gamma M^4 = \frac{\mu_0H}{M}. \quad (2)$$

The parameter β can be negative or positive describing a FOMT or SOMT, respectively. Fine-tuning the character of the magnetic transition towards the critical point between FOMT and SOMT ($\beta = 0$) could be an essential step to achieve the best compromise of maximizing the efficiency for applications while keeping a reversible process to ensure longevity of the MCE material.

Promising MCE materials are $(\text{Mn, Fe})_2(\text{P, Si, B})$ compounds [3, 16], which combine tunable Curie temperatures and

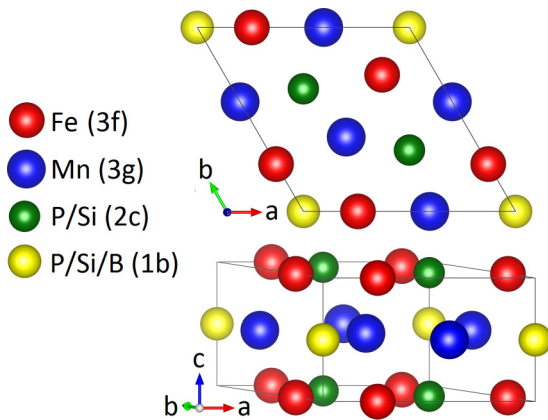


FIG. 1. Hexagonal unit cell ($P\bar{6}2m$) of $MnFe(P, Si, B)$. Fe and Mn preferably occupy the $3f$ and $3g$ Wyckoff positions, respectively. The $1b$ and $2c$ positions are occupied by P and Si. B substitutes P on the $1b$ position.

large magnetization changes. $(Mn, Fe)_2(P, Si, B)$ crystallizes in a hexagonal crystal structure (space group $P\bar{6}2m$) with two layers, where the magnetic atoms Fe and Mn preferably occupy the crystallographic $3f$ ($x_f, 0, 0$) and $3g$ ($x_g, 0, 1/2$) Wyckoff positions [17,18], respectively. (Fig. 1, drawn by VESTA [19].)

Neutron diffraction shows that all the magnetic moments in the $(Mn, Fe)_2(P, Si)$ series are aligned in the ab plane until Fe is completely replaced by Mn [17]. In the ferromagnetic state the $3g(Mn)$ moments remain constant at about $2.6 \mu_B$, while the $3f(Fe)$ linearly decrease from 1.5 to $0.4 \mu_B$ with increasing Mn content [17].

The nonmagnetic atoms P and Si occupy the $1b$ ($0, 0, 1/2$) and $2c$ ($1/3, 2/3, 0$) site [20]. Boron preferably occupies the $1b$ site [21,22].

The MCE in $(Mn, Fe)_2(P, Si, B)$ compounds originate from the interplay between the two magnetic layers with magnetic atoms on the crystallographic $3g$ and $3f$ site, respectively. This so-called “mixed magnetism” [3] is governed by *strong magnetism* ($3g$ site) and *weak magnetism* ($3f$ site). The magnetic moment on the $3g$ site stays relatively stable across the transition, whereas the moment on the $3f$ site is strongly reduced in magnitude when the paramagnetic phase is entered. This strong reduction in the magnetic moment on the $3f$ site is attributed to covalent bond formation with the nonmagnetic atoms in the paramagnetic state [23,24]. The mechanism driving the character of the ferromagnetic magnetoelastic transition, and consequently the magnetic entropy change, is still not fully understood in these compounds as systematic studies on the charge redistribution across the ferromagnetic transition with samples gradually changing from a FOMT towards a SOMT were unavailable.

Our main goal is to explore the driving forces in $(Mn, Fe)_2(P, Si, B)$ compounds that define the character of the magnetoelastic transition. Therefore, we gradually tuned the magnetic transition from a strong first-order towards a second-order character by incrementally substituting P by B. We studied the correlations between magnetic and structural properties across T_C and investigated how the electron

density redistribution develops across T_C , when the magnetic character is tuned stepwise from a FOMT towards a SOMT. Our investigation aims at identifying the nature of the magnetic phase transition to be able to better design suitable MCE materials for magnetic cooling, heat pumps, and magnetic energy conversion. Our interest is to identify the essential parameters controlling the strength of the MCE and consequently the change in magnetization across the transition.

II. EXPERIMENT

The five studied samples were $Mn_1Fe_1P_{0.6-w}Si_{0.4}B_w$ with $w = 0, 0.02, 0.04, 0.06, \text{ and } 0.08$. We mixed powders of Mn, Fe, P, Si, and B via ball milling for 10 h at 380 rounds per min. The resulting powders were pressed into cylindrical tablets, which were sealed in quartz tubes in Ar atmosphere and then annealed for 25 h at 1100°C . Temperature-dependent magnetization was measured in a magnetometer equipped with a superconducting quantum interference device (SQUID, Quantum Design MPMS 5XL). We determined magnetic entropy changes by field-dependent isothermal magnetization measurements utilizing the Maxwell relations. High-resolution x-ray diffraction was performed at the BM01A beamline at the European Synchrotron Radiation Facility (ESRF) using a wavelength of 0.69264 \AA . The measurement covered a temperature range from 150 to 500 K in temperature steps of 2 K. The temperature was controlled by a Nitrogen Cryostream. The samples were put in capillaries with 0.5 mm diameter and spun. Diffraction data were analyzed by Rietveld refinement using the FULLPROF Suite [25]. Electron densities were calculated by VESTA [19] and processed in MATLAB [26].

III. RESULTS

A. Magnetic properties

The temperature dependent magnetization of $Mn_1Fe_1P_{0.6-w}Si_{0.4}B_w$ was measured in a magnetic field of 1 T and shows increasing T_C 's (heating) ranging from 281 to 330 K for $w = 0$ and $w = 0.08$, respectively [Fig. 2(a)]. The largest thermal hysteresis of $\Delta T_{hys} = 54 \text{ K}$ is observed for the sample with no B ($w = 0$). The hysteresis gradually decreases with increasing B content and practically disappears in the sample with $w = 0.08$.

The magnetic entropy change $-\Delta S$ was determined in magnetic fields up to 2 T [Fig. 2(b)]. In a magnetic field of 1 T $Mn_1Fe_1P_{0.6}Si_{0.4}$ ($w = 0$) shows a maximum of $-\Delta S = 6.7 \text{ J kg}^{-1} \text{ K}^{-1}$ at T_C . An increasing B content leads to an increase in magnetic entropy change with a maximum of $-\Delta S = 13.1 \text{ J kg}^{-1} \text{ K}^{-1}$ for $w = 0.06$. For $w = 0.08$ the entropy change slightly drops to $-\Delta S = 6.8 \text{ J kg}^{-1} \text{ K}^{-1}$.

B. Structural properties

The intensity distribution for scattering angles 2θ from 17° to 21° as a function of temperature are shown in Figs. 3(a)–3(e). The peak intensities of the main peaks are represented in a color-coded contour plot. We observe clear discontinuous jumps in the diffraction peaks across the ferromagnetic transition for the samples with $w = 0$ – 0.06 (e.g.

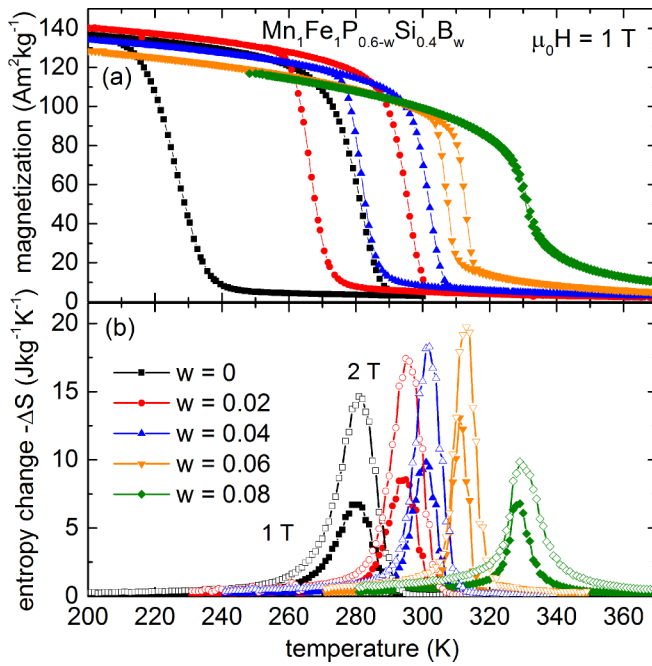


FIG. 2. (a) Temperature dependent magnetization for $\text{Mn}_1\text{Fe}_1\text{P}_{0.6-w}\text{Si}_{0.4}\text{B}_w$ ($w = 0, 0.02, 0.04, 0.06, \text{ and } 0.08$) obtained in a magnetic field of $\mu_0 H = 1 \text{ T}$ and (b) magnetic entropy changes $-\Delta S$ for 1 T (filled symbols) and 2 T (open symbols).

see the $\{210\}$ diffraction peak). Furthermore, we observe a small temperature interval, where ferromagnetic and paramagnetic phase coexist. Both observations are characteristic for a material with a FOMT character. The weak peak close to 20° corresponds to the $\{220\}$ reflection of the impurity phase $(\text{Mn}, \text{Fe})_3\text{Si}$. This phase occurs in all samples, however only in small amounts ($<10\%$). The diffraction pattern of $(\text{Mn}, \text{Fe})_3\text{Si}$ shows no significant changes with temperature and posed no problem for the analysis of the main phase. With increasing B content the discontinuous steps in the scattering angle of the main reflections at T_C become smaller and are nearly continuous for the sample with largest B content ($w = 0.08$). Such a behavior indicates a weak FOMT (close to the critical point) being on the verge of a SOMT. Figures 3(f)–3(j) shows the corresponding low temperature data and Rietveld refinements for all samples at 150 K.

The obtained changes in lattice parameters and unit cell volume with temperature are shown in Figs. 3(k)–3(n). The in-plane lattice parameter a shows a jump and decreases upon heating across T_C [Fig. 3(k)]. On the other hand, the out-of-plane lattice parameter c shows the opposite behavior and exhibits a steep increase upon heating across T_C [Fig. 3(l)]. The c/a ratio as a function of temperature increases with increasing B content [Fig. 3(m)]. The jumps across T_C in lattice parameters are largest in the sample with $w = 0$ and gradually become smaller with increasing B content.

In addition to the main phase $\text{Mn}_1\text{Fe}_1\text{P}_{0.6-w}\text{Si}_{0.4}\text{B}_w$ we detect the $(\text{Mn}, \text{Fe})_3\text{Si}$ impurity phase in all samples. The amount of impurity phase gradually increases with increasing B content from 6% for $w = 0$ and reaches a maximum value of 10% for $w = 0.06$.

C. Internal coordinates of Fe and Mn

We observe shifts in the internal coordinates of the $3g$ and $3f$ Wyckoff positions within the unit cell across T_C (Fig. 4). The $3g$ and $3f$ sites are preferably occupied by Mn and Fe, respectively. The largest discontinuous shift upon heating are observed in the sample without B ($w = 0$). With increasing B content the jumps in both internal coordinates at T_C become smaller. For $w = 0.08$ we observe a gradual continuous decrease of the internal coordinates upon heating. Close to the magnetic transition the uncertainties in the Rietveld refinement increase in the “two-phase region” due to the coexistence of the ferro- and paramagnetic phase leading to a strong overlap of peaks with reduced phase fractions. We removed the data within the two-phase region, where the refinements exhibited large uncertainties.

D. Electronic structure

The high-resolution diffraction data can be used to extract the electron densities from the structure factors obtained from the refinement. The structure factors from the model obtained in the refinement were further processed with VESTA [19], which performs the Fourier transformation and calculates the electron densities. In order to highlight changes in the electron density across T_C we created electron density difference plots by subtracting the ferromagnetic from the paramagnetic state (PM–FM) after normalization. The unit cells were presented in relative lattice units to subtract the phases. We assumed a constant unit cell charge at all temperatures. The diffracted intensity does however decrease with increasing temperature due to increased thermal motions of the atoms. In order to maintain a constant sum of all structure factors we multiplied the structure factors by a temperature-dependent correction factor and normalized the data. The same method has been successfully applied in our previous investigations (for more details see Refs. [23,24]). Here we investigate the electron density of the $3f(\text{Fe})$ and the $3g(\text{Mn})$ site for a series of samples with varying entropy change at T_C .

The color-coded electron density difference plots within the a - b plane between paramagnetic (500 K) and ferromagnetic (150 K) state for $\text{Mn}_1\text{Fe}_1\text{P}_{0.6-w}\text{Si}_{0.4}\text{B}_w$ ($w = 0$ – 0.08) are shown for the $3f$ site [Figs. 5(a)–5(e)] and the $3g$ site [Figs. 5(f)–5(j)] containing the Fe and Mn atoms, respectively. In order to emphasize the effects originating from the different magnetic atoms, we only consider the local environment close to the $3f(\text{Fe})$ and $3g(\text{Mn})$ sites and chose different integration boundaries for the layers containing the $3f$ and $3g$ sites: the integration along the c axis in internal coordinates of the unit cell has been performed from $z = -0.25$ to 0.25 for the Fe layer ($3f$ site) and from $z = 0.25$ to 0.75 for the Mn layer ($3g$ site). Furthermore, the shift in internal coordinates with temperature is removed by applying corresponding shifts given in Fig. 4, in order to emphasize on the effects originating from redistribution of electron densities across the magnetic transition.

The electron density difference between the paramagnetic and ferromagnetic state corresponds to positive (red) and negative (blue) values, respectively. We applied the same scale in $\text{e}\text{\AA}^{-3}$ for all electron density difference

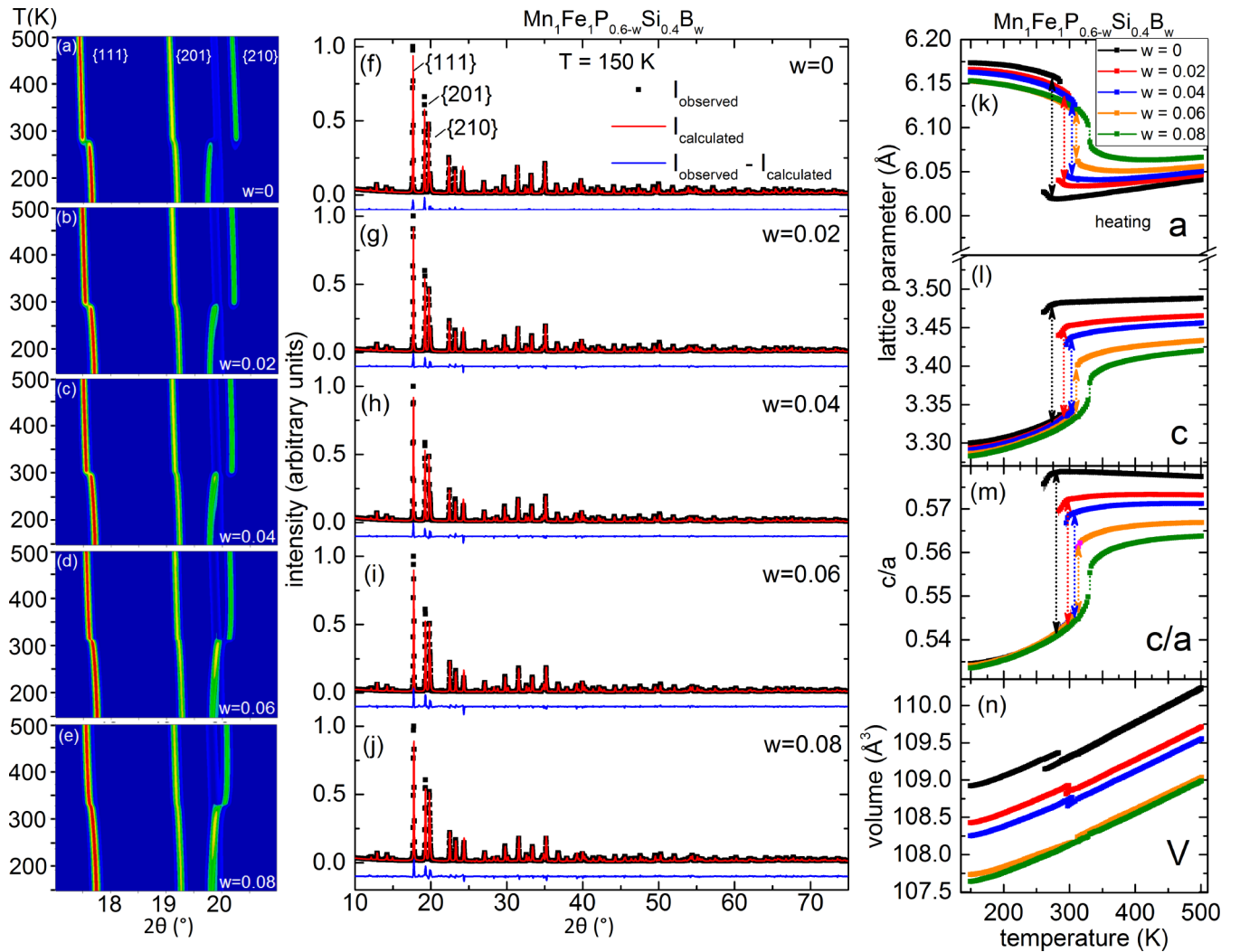


FIG. 3. (a)–(e) Intensity versus scattering angle 2Θ ($^\circ$) as a function of temperature T (K) for $\text{Mn}_1\text{Fe}_1\text{P}_{0.6-w}\text{Si}_{0.4}\text{B}_w$ ($w = 0, 0.02, 0.04, 0.06, \text{ and } 0.08$) obtained in high-resolution x-ray powder diffraction measurements. The $\{111\}$ and $\{210\}$ diffraction peaks are shown across the ferromagnetic-paramagnetic transition upon heating. (f)–(j) x-ray diffraction patterns and Rietveld refinements for $w = 0$ – 0.08 measured at 150 K. Temperature dependence upon heating of (k)–(l) hexagonal lattice parameters, (m) c/a ratio and (n) the unit cell volume. The low intensity peak close to 20° corresponds to the $\{220\}$ reflection of the impurity phase $(\text{Mn}, \text{Fe})_3\text{Si}$.

plots for comparison. The evolution of electron density difference with changing temperature interval for $w = 0$ (Fig. S1) and $w = 0.08$ (Fig. S2) is given in the supplementary material [27].

We observe the strongest changes in the electron density around the $3f(\text{Fe})$ as well as $3g(\text{Mn})$ site for the sample without B ($w = 0$) with changes ranging from $-19\text{e}\text{\AA}^{-3}$ to $+4\text{e}\text{\AA}^{-3}$. Substitution of B has a profound effect on the electronic structure and strongly weakens the electronic redistribution across the magnetic transition. The changes in the electron density difference for $w = 0.02$ – 0.08 across T_C is reduced by a factor of 3–5 compared to $w = 0$. Furthermore, the lowest changes in the electron density difference occur in the sample with $w = 0.02$ and then gradually increase with increasing B content. We also observe qualitative differences in the redistribution of electron density across T_C . The redistribution of electron density around the Fe site ($3f$) shows strong localization in the paramagnetic state (red) pointing to-

wards other nearest neighbor Fe sites and the $2c$ sites indicated by black lines and white lines in Fig. 5(a), respectively. On the other hand, the redistribution in the paramagnetic state around the Mn site is more uniform and does not show a sizable directional character. This localization on the $3f$ (Fe) site and the more uniformly distributed electron density on the $3g$ (Mn) site in the paramagnetic state can be observed in all samples. However, electron density redistribution of the sample without B ($w = 0$) is set apart from the other samples, due to its steep increase in electronic changes, which are much stronger compared to all other samples that contain B.

The color-coded electron density difference plots in Fig. 5 show a selected range around the magnetic atoms. By considering the close environment of one crystallographic site it is possible to remove the effect of the shift in internal coordinates (see Fig. 4) with temperature and only visualize the electronic redistribution.

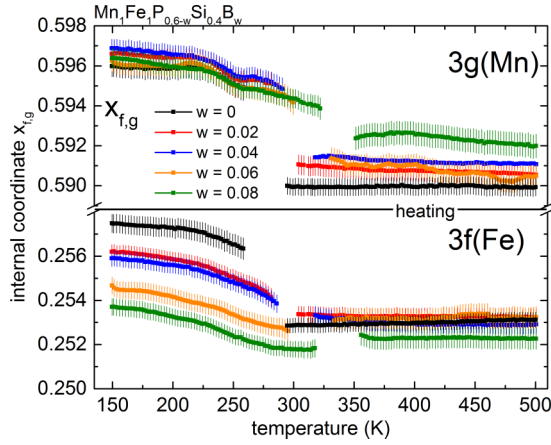


FIG. 4. Temperature dependence of the internal coordinates of the $3f(\text{Fe})$ and $3g(\text{Mn})$ position for $\text{Mn}_1\text{Fe}_1\text{P}_{0.6-w}\text{Si}_{0.4}\text{B}_w$ ($w = 0-0.08$) across T_C upon heating.

IV. DISCUSSION

In order to identify trends in our series of samples, we summarize the magnetic (T_C , ΔT_{Hys}) and structural [$\Delta(c/a)/(c/a)$, $x_{f,g}$] properties as function of B content in Fig. 6.

A. Magnetic and structural properties

Substitution of B in $\text{Mn}_1\text{Fe}_1\text{P}_{0.6-w}\text{Si}_{0.4}\text{B}_w$ ($w = 0-0.08$) has a systematic impact on the magnetic properties. In particular, the transition gradually changes from a FOMT towards a SOMT. Decreasing discontinuous jumps in lattice parameters [Fig. 3(k)-3(l)] across T_C systematically weaken the FOMT and lead to a systematic increase of the magnetic transition temperatures [Fig. 7(a)] with a decrease in hysteresis [Fig. 7(b)]. The hysteresis becomes practically zero for $w = 0.08$ indicating a near SOMT character.

The gradual changes in T_C and hysteresis with B substitution are also reflected in the structural properties. With increasing B content the discontinuous jump across T_C in lattice parameters and c/a ratio ($\Delta(c/a)/(c/a)$) gradually becomes smaller [Fig. 7(d)]. Furthermore, we observe a gradual shift in internal coordinates of the $3f(\text{Fe})$ and $3g(\text{Mn})$ position between 500 and 150 K with increasing B content [Fig. 7(e)].

On the other hand, the maximum of the magnetic entropy change $-\Delta S_m$ at T_C [Fig. 7(c)] does not show a similar clear trend with increasing B content. The entropy change $-\Delta S_m$ increases from $w = 0$, has a maximum at $w = 0.06$ and shows a decrease for $w = 0.08$. This behavior resembles the trend observed in the impurity phase content. A systematic study of how the impurity phase content is related to the magnetic entropy change across the $(\text{Mn}, \text{Fe})_2(\text{P}, \text{Si})$ family is outside the scope of this investigation.

B. Electron density difference plots

The electron density difference plots only reveal systematic evolution for the samples containing B ($w = 0.02-0.08$), where the electronic distribution between 150 and 500 K does not show significant changes on the $3f(\text{Fe})$ and $3g(\text{Mn})$ site

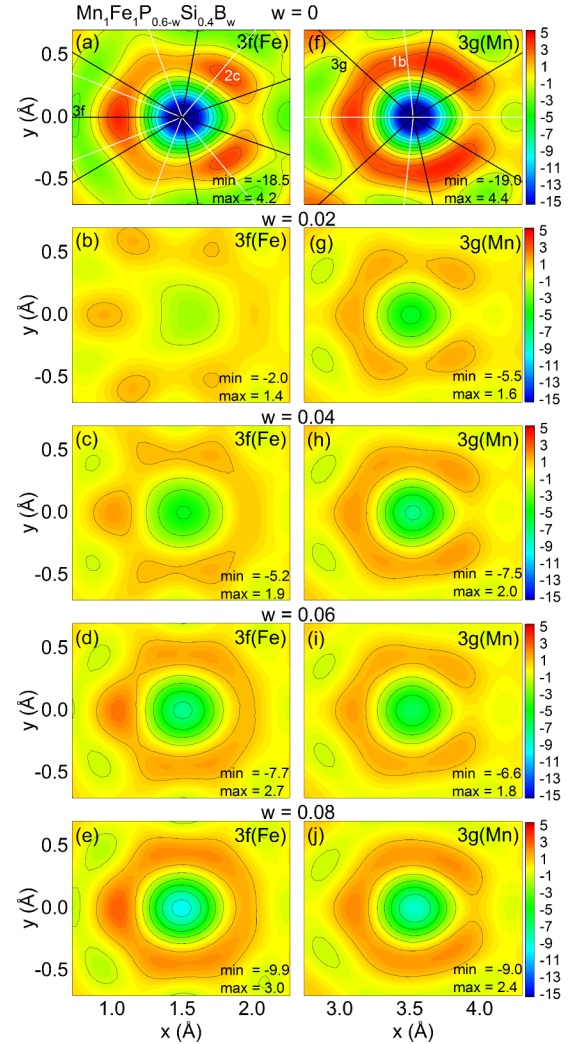


FIG. 5. Electron density difference plots between PM (500 K) and FM (150 K) phase (PM-FM) in the local environment of the (a)-(e) $3f$ and (f)-(j) $3g$ sites for $\text{Mn}_1\text{Fe}_1\text{P}_{0.6-w}\text{Si}_{0.4}\text{B}_w$ ($w = 0-0.08$). The electron densities were integrated from $z = -0.25$ to 0.25 and $z = 0.25$ to 0.75 (internal coordinates) for $3f(\text{Fe})$ and $3g(\text{Mn})$ positions, respectively. The shift of internal coordinates with temperature is removed by the corresponding shifts from Fig. 4 in order to emphasize the effects originating from redistribution of electron densities. The color-coded scale is given in $e\text{\AA}^{-3}$.

[Fig. 7(f)]. However, we observe strongly increased changes in the electron density across T_C for the sample without B ($w = 0$). Small amounts of B seem to significantly disturb the overall distribution of the electron density across the whole unit cell and lead to a strongly reduced change in the electron density compared to the parent compound without B.

The substitution of B and the associated reduction of the number of electrons in the unit cell seem to strongly suppress the electronic changes across the transition. X-ray absorption and x-ray magnetic circular dichroism measurements on $(\text{Mn}, \text{Fe})_2(\text{P}, \text{Si}, \text{B})$ compounds [16] reveal large changes at the phosphorous K edge across the magnetic transition, which indicates an electronic reconstruction. This feature is accompanied by large changes in the interatomic distances between,

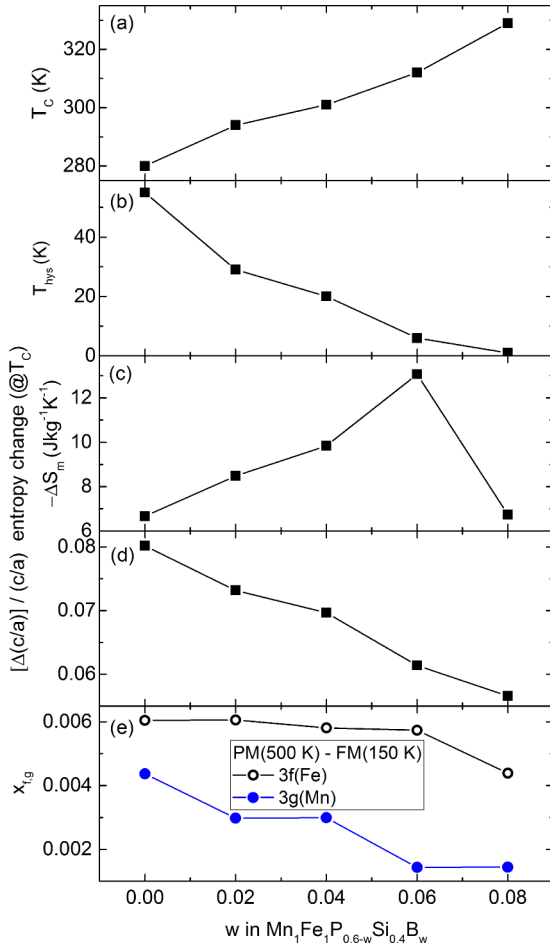


FIG. 6. (a) Curie temperature T_C , (b) thermal hysteresis ΔT_{hys} , (c) maximum magnetic entropy change, (d) change of c/a ratio in respect to 150 K $\Delta(c/a)/(c/a)$, and (e) internal coordinate of the $3f$ (Fe) and $3g$ (Mn) position within the unit.

e.g., the $3g$ (Mn) and $1b$ (P,Si,B) sites across the transition and linked to changes in metal-metalloid bonding. The amplitude of this effect is correlated to the discontinuity in interatomic distances at the transition and is strongly reduced by boron substitution. All samples show a localized redistribution on the $3f$ (Fe) site.

However, the strong electronic changes for $w = 0$ compared to the series of samples that contain B is, however, not reflected in the magnetic and the structural properties.

Strong localization of the electron density in the paramagnetic state of the Fe site pointing to other Fe atoms and the P/Si atoms indicate bond formation, which leads to a reduced magnetic moment on the Fe site above T_C , which has been reported in our previous investigations [24]. Furthermore, our measurements reveal that the electron density changes across T_C are more evenly distributed around the Mn-site. The Mn site does not show indications of bond formation, which is consistent with the observation that the magnetic moment keeps its value across T_C . [17].

For a SOMT, the changes in the electron density, magnetic, and structural properties are extended over a larger temperature range compared to a FOMT. It is expected that short-range magnetic order exists in a SOMT sample in the

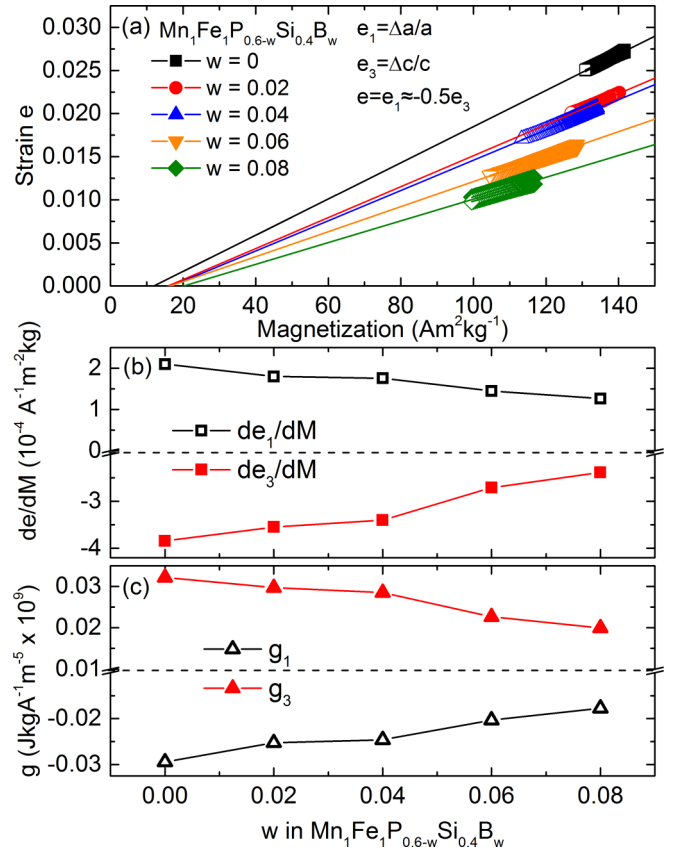


FIG. 7. (a) Strain $e = e_1 = -\frac{1}{2}e_3$ with $e_1 = \frac{\Delta a}{a}$ and $e_3 = \frac{\Delta c}{c}$ in the ferromagnetic phase of $\text{Mn}_1\text{Fe}_1\text{P}_{0.6-w}\text{Si}_{0.4}\text{B}_w$ ($w = 0-0.08$) as function of the magnetization. From (a) linear fits indicated by solid lines we obtain (b) the slope $de_{1,3}/dM$, which is used to calculate (c) the magnetoelastic coupling constants g_1 (in ab -plane) and g_3 (out of plane along the c axis). Dashed black lines in (b) and (c) mark breaks in the vertical axis.

paramagnetic state, which continuously develops into long-range magnetic order by cooling below the magnetic transition temperature. The electron density stays relatively constant above T_C in the samples with B ($w = 0.02-0.08$), which indicates that no significant short-range order is present. However, the sample without B ($w = 0$) exhibiting the strongest FOMT shows that the changes in the electron density difference still weakly increase with heating above T_C .

The changes in the electronic structure with increasing B content can be related to the mechanical properties. A previous study showed a strong increase in ductility, when B was present in the sample [28]. A systematic study of the ductility and the evolution of electron densities across T_C with changing B content would be desirable to investigate a possible correlation between both properties.

C. Magnetoelastic coupling

The change in lattice parameters across the magnetic transition is closely related to the elastic strain in the material. In the ferromagnetic state it is energetically favorable to induce elastic strains and thereby deform the structure. We determined the strain and magnetoelastic coupling constants

for all samples, which is explained in detail in our previous investigation [24]. Including the elastic energy and magnetoelastic coupling we obtain for the Gibbs free energy

$$\Delta G = \frac{\alpha}{2}M^2 + \frac{\beta}{4}M^4 + \frac{\gamma}{6}M^6 - \mu_0HM + \frac{1}{2} \sum_{i,j} C_{ij}e_i e_j + \sum_i g_i e_i M, \quad (3)$$

where C_{ij} are the elastic constants, e_i is the elastic strain, and g_i are the magnetoelastic coupling constants. Considering a hexagonal symmetry, the tensile strains within the basal plane is $e_1 = \Delta a/a$ and along the sixfold axis $e_3 = \Delta c/c$. Minimization of ΔG with respect to the strains ($d\Delta G/de_1 = 0$ and $d\Delta G/de_3 = 0$) results in

$$(C_{11} + C_{12})e_1 + C_{13}e_3 + g_1M = 0, \quad (4)$$

$$2C_{13}e_1 + C_{33}e_3 + g_3M = 0. \quad (5)$$

The strain as function of magnetization is shown in Fig. 7(a). The volume change across the transition is tuned to be small [see Fig. 3(n)]. Therefore, we can simplify the analysis by defining that $e \equiv e_1 = -\frac{1}{2}e_3$ (see also Ref. [24]). By using the derivatives de_1/dM and de_3/dM [Fig. 7(b)] and taking the elastic constants from Ref. [29], we can calculate the magnetoelastic coupling constants within the plane $g_1 = -(C_{11} + C_{12} - 2C_{13})de_1/dM$ and along the sixfold axis $g_3 = -(C_{33} - C_{13})de_3/dM$ shown in Fig. 7(c). The elastic constants are $C_{11} = 308.4$, $C_{12} = 120.0$, $C_{13} = 144.0$, $C_{33} = 227.8$, $C_{44} = 119.5$, and $C_{66} = 94.2$ GPa [29].

The strongest magnetoelastic coupling leading to the highest energy gain in the Gibbs free energy is present in the sample without B ($w = 0$), which has the strongest FOMT character. The magnetoelastic coupling constants gradually change and values approach each other when the samples are tuned with an increasing B content towards the SOMT. In contrast to the electron density difference, the sample without

B follows the same trend as the other samples containing B for the magnetoelastic coupling. The average of the magnetoelastic coupling constants for all samples in the series are $g_1 = -0.023 \times 10^9 \text{ J kg A}^{-1} \text{ m}^{-5}$ and $g_3 = -0.027 \times 10^9 \text{ J kg A}^{-1} \text{ m}^{-5}$ with an experimental ratio of $(\frac{g_3}{g_1})_{\text{exp}} = -1.13$. This experimental ratio is in close agreement with the theoretical value for $e_1 = -\frac{1}{2}e_3$ predicted by the Landau model: $(\frac{g_3}{g_1})_{\text{th}} = -2(C_{33} - C_{13})/(C_{11} + C_{12} - 2C_{13}) = -1.19$.

For all samples ($w = 0-0.08$), we observe similar gradual trends between the change of lattice parameters, the magnetoelastic coupling, the transition temperature T_C , and thermal hysteresis (Fig. 7). Our investigation indicates that the magnetoelastic coupling strength is closely linked to the transition temperature and hysteresis in this series. By controlling the B content the jump in lattice parameters across T_C can be tuned to minimize the hysteresis and improve the ductility.

V. CONCLUSIONS

By systematically increasing the B content, the magnetization, thermal hysteresis, lattice constants, and internal coordinates of Mn and Fe consistently evolve. Localized changes in electron density at the Fe site, indicate bond formation. Electron density changes across T_C are more evenly distributed on the Mn site. Substitution of B has a significant impact on the electron density and bond formation. The sample without B shows significantly larger changes in the electron density across T_C compared to all samples with B substitution. On the other hand, the magnetoelastic coupling shows a continuous weakening with increasing B content. We observe a clear trend, that a decreasing jump in the lattice parameters across the magnetic transition enhances T_C and decreases hysteresis.

ACKNOWLEDGMENTS

The authors thank the beamline staff at the Swiss-Norwegian Beam Lines (BM01) at ESRF and Anton Lefering for their technical support. This work was financially supported by TKI Urban Energy with Project No. 163GM06.

-
- [1] H. Yibole, F. Guillou, L. Caron, E. Jiménez, F. M. F. de Groot, P. Roy, R. de Groot, N. H. van Dijk, and E. Brück, *Phys. Rev. B* **91**, 014429 (2015).
- [2] F. Guillou, H. Yibole, G. Porcari, L. Zhang, N. H. van Dijk, and E. Brück, *J. Appl. Phys.* **116**, 063903 (2014).
- [3] N. H. Dung, Z. Q. Ou, L. Caron, L. Zhang, D. T. C. Thanh, G. A. de Wijs, R. A. de Groot, K. H. J. Buschow, and E. Brück, *Adv. Energy Mater.* **1**, 1215 (2011).
- [4] O. Tegus, E. Brück, K. H. J. Buschow, and F. R. de Boer, *Nature (London)* **415**, 150 (2002).
- [5] K. A. Gschneidner and V. K. Pecharsky, *Int. J. Refrig.* **31**, 945 (2008).
- [6] L. Caron, X. F. Miao, J. C. P. Klaasse, S. Gama, and E. Brück, *Appl. Phys. Lett.* **103**, 112404 (2013).
- [7] N. V. Thang, X. F. Miao, N. H. van Dijk, and E. Brück, *J. Alloy. Compd.* **670**, 123 (2016).
- [8] <http://www.swiss-blue-energy.ch/>.
- [9] T. Christiaanse and E. Brück, *Met. Mater. Trans. E* **1**, 36 (2014).
- [10] D. Vuarnoz, A. Kitanovski, C. Gonin, and P. W. Egolf, *Int. J. Energy* **10**, 365 (2012).
- [11] D. Vuarnoz, A. Kitanovski, C. Gonin, Y. Borgeaud, M. Delessert, M. Meinen, and P. W. Egolf, *Appl. Energy* **100**, 229 (2012).
- [12] L. D. Kirol and J. I. Mills, *J. Appl. Phys.* **56**, 824 (1984).
- [13] L. Brillouin and H. P. Iskenderian, *Electr. Commun.* **25**, 300 (1948).
- [14] M. Fries, Z. Gercsi, S. Ener, K. P. Skokov, and O. Gutfleisch, *Acta Mater.* **113**, 213 (2016).
- [15] A. M. G. Carvalho, A. A. Coelho, S. Gama, F. C. G. Gandra, P. J. von Ranke, and N. A. de Oliveira, *Eur. Phys. J. B* **68**, 67 (2009).
- [16] F. Guillou, K. Ollefs, F. Wilhelm, A. Rogalev, A. N. Yaresko, H. Yibole, N. H. van Dijk, and E. Brück, *Phys. Rev. B* **92**, 224427 (2015).

- [17] N. H. Dung, L. Zhang, Z. Q. Ou, L. Zhao, L. van Eijck, A. M. Mulders, M. Avdeev, E. Suard, N. H. van Dijk, and E. Brück, *Phys. Rev. B* **86**, 045134 (2012).
- [18] Z. Q. Ou, L. Zhang, N. H. Dung, L. van Eijck, A. M. Mulders, M. Avdeev, N. H. van Dijk, and E. Brück, *J. Magn. Magn. Mater.* **340**, 80 (2013).
- [19] K. Momma and F. Izumi, *J. Appl. Crystallogr.* **44**, 1272 (2011).
- [20] X. F. Miao, L. Caron, P. Roy, N. H. Dung, L. Zhang, W. A. Kockelmann, R. A. de Groot, N. H. van Dijk, and E. Brück, *Phys. Rev. B* **89**, 174429 (2014).
- [21] X. F. Miao, N. V. Thang, L. Caron, H. Yibole, R. I. Smith, N. H. van Dijk, and E. Brück, *Scripta Mater.* **124**, 129 (2016).
- [22] F. Guillou, H. Yibole, G. Porcari, and E. Brück, *Phys. Status Solidi C* **11**, 1007 (2014).
- [23] M. F. J. Boeije, P. Roy, F. Guillou, H. Yibole, X. F. Miao, L. Caron, D. Banerjee, N. H. van Dijk, R. A. de Groot, E. Brück, *Chem. Mater.* **28**, 4901 (2016).
- [24] M. F. J. Boeije, M. Maschek, X. F. Miao, N. V. Thang, N. H. van Dijk, and E. Brück, *J. Phys. D: Appl. Phys.* **50**, 174002 (2017).
- [25] <https://www.ill.eu/sites/fullprof/>.
- [26] T. M. matlab and Statistics Toolbox Release 2014b, Inc., Natick, Massachusetts, United States.
- [27] See Supplemental Material at <http://link.aps.org/supplemental/10.1103/PhysRevB.98.224413> for electron density difference plots for different temperature intervals for $\text{Mn}_1\text{Fe}_1\text{P}_{0.6}\text{Si}_{0.4}$ and $\text{Mn}_1\text{Fe}_1\text{P}_{0.52}\text{Si}_{0.4}\text{B}_{0.08}$.
- [28] F. Guillou, H. Yibole, N. H. van Dijk, L. Zhang, V. Hardy, and E. Brück, *J. Alloy. Compd.* **617**, 569 (2014).
- [29] P. Roy, E. Torun, and R. A. de Groot, *Phys. Rev. B* **93**, 094110 (2016).